

Nanosheet-assembled hollow NiO ball-flower for high-performance supercapacitor

Jinxing Wang¹ · Yangyang Zhang¹ · Piaopiao Wan¹ · Tianming Li¹ · Dewen Hou¹ · Shahid Hussain¹ · Hongyan Shao¹

Received: 27 February 2016 / Accepted: 7 April 2016 / Published online: 12 April 2016
© Springer Science+Business Media New York 2016

Abstract Hollow NiO ball-flowers closely assembled by porous nanosheets have been synthesized via a simple and template-free hydrothermal method. When applied to supercapacitor as electrode materials, the as-prepared NiO ball-flowers with hierarchical, porous, and hollow structures exhibited high specific capacitance value (734 F g^{-1}) at a current density (1 A g^{-1}), as well as good cycling stability. The outstanding electrochemical performance may be attributed to the morphology and structure of the nanosheet-assembled hollow ball-flowers which have the advantages of increasing specific surface area, facilitating the contact between the electrode and electrolyte, and accommodating the volume changes during faradaic reaction.

1 Introduction

Nickel oxide (NiO), as the pseudo-capacitive electrode materials, owing to its high theoretical specific capacitance of 2573 F g^{-1} , availability, environmental-friendly and low cost [1–3], has shown considerable promise for supercapacitor. However, the challenges in using NiO electrode materials for supercapacitor including the relatively low actual specific capacitance, poor cycle performance and high resistivity need to be solved urgently [2, 4].

Currently, it is suggested the poor electrochemical performance of electrode materials may be overcome by

designing proper nanostructures such as the hierarchical and porous structure [5], hollow nanospheres [6], porous nanotube arrays [7], suitable pore size [8], surface feature [9, 10], etc. Considerable researches have demonstrated that increasing the porosity could be an effective way to obtain high specific surface area for effective contact between active materials and electrolyte, as well as to shorten ion/electron diffusion distance, which are the key points to improve the electrochemical performance [5, 11, 12]. Besides, the hierarchical porous systems of electrode materials make it more difficult for aggregation compared with nanoparticles, and provide numerous open spaces buffering the volume variation during the faradaic reaction [9, 11]. In addition to the porosity and hierarchical structures, the hollow structure often provides much more cavities acting as an “ion reservoir” and sufficient space for lattice expansion [9, 13]. Many previous results demonstrate that these particular architectural features are so critical to improve the electrochemical performance of active materials [1, 6, 14]. However, most of porous, hierarchical and hollow architectures were synthesized by complicated chemistry process and usually the template is necessary to preparation [9, 15, 16]. So far there is little report about the high-performance supercapacitors base on the NiO electrode materials with hierarchical, porous, and hollow structures.

In this paper, hollow hierarchical NiO ball-flowers closely assembled by porous nanosheets for one-step synthesis were developed. This unique structure with a large specific surface area of $163.1 \text{ m}^2 \text{ g}^{-1}$ has the unimpeded ion/electron diffusion channel and ubiquitous chambers which can serve as the “ion reservoir” improving the electrochemical performance. Consequently, the hollow NiO ball-flowers exhibit excellent electrochemical properties and have promising applications.

✉ Jinxing Wang
wjx@cqu.edu.cn

¹ College of Materials Science and Engineering, Chongqing University, Chongqing 400030, China

2 Experimental

2.1 Synthesis of NiO hollow ball-flowers

All of the reagents in the experiments were analytical grade and used directly without purification. In a typical experimental procedure, 2.62 g of $\text{NiSO}_4 \cdot 6\text{H}_2\text{O}$ was dissolved in 30 mL of deionized water. Then, 0.8 g of NaHCO_3 was added to the obtained solution. After stirring for 30 min, 1.40 g of HMT (hexamethylenetetramine) was added to the above mixed solution under stirring. After complete dissolution, the mixture was pipetted into a 50-mL Teflon-lined stainless autoclave which subsequently heated at 110 °C for 6 h. After that, the product was washed with deionized water and ethanol for several times. Finally, the powder was dried at 60 °C for 12 h and then was annealed at 400 °C in air for 3 h.

2.2 Structural characterization

The as-prepared product was characterized by X-ray diffractometer (XRD, D/max-1200X with Cu $K\alpha$ radiation). The morphology of the sample was examined with a focused ion beam field emission scanning double beam electron microscopy (Zeiss Auriga FIB/SEM) and a transmission electron microscope (TEM, Zeiss, Libra200) respectively. The surface area and pore-size distribution of the as-synthesized material were measured by Brunauer–Emmett–Teller (BET) and Barrett–Joyner–Halenda (BJH) methods (Micromeritics, ASAP2020).

2.3 Electrochemical measurements

The electrochemical performances were measured in a three electrode electrochemical workstation (RST 5100F, Zheng Zhou) with 6 M KOH aqueous solution as the electrolyte. Working electrodes were prepared by mixing the as-synthesized NiO powder (70 wt%) with acetylene black (20 wt%), and polytetrafluoroethylene (PVDF) binder (10 wt%) in *N*-methyl-pyrrolidone (NMP) to form a slurry, then the mixture was coating onto the surface of nickel foam current collectors (1.0 cm × 1.0 cm) and dried at 60 °C for 4 h. Saturated calomel electrode (SCE) and platinum plate were used as reference and counter electrode, respectively. Cyclic voltammetry (CV) measurement was performed in potential window of 0–0.6 V (vs. SCE), at the scan rates of 5–50 mV s⁻¹. Galvanostatic charge–discharge (GCD) testing was conducted at different current densities from 1 to 20 A g⁻¹ between 0 and 0.45 V. The electrochemical impedance spectroscopy (EIS) was evaluated in the frequency range from 0.1 Hz to 10 kHz at a potential amplitude of 5 mV.

3 Results and discussion

3.1 Structure and morphology

Figure 1a shows the XRD pattern of NiO hollow ball-flower. All the identified peaks located at 37.2°, 43.3°, 62.9°, 75.4° and 79.4° could be well assigned to the (111), (200), (220) (311) and (222) planes of cubic structured NiO (JCPDS card no. 47-1049) without any additional diffraction peaks, suggesting high purity of the as-synthesized NiO.

Figure 1b shows the SEM image of the as-prepared sample NiO, it can be seen that the microspheres are monodispersed and uniform with diameters range from 2 to 5 μm. It is obvious that these microspheres are with hollow cavities (arrows in Fig. 1b point to the hollow cavities). From Fig. 1c, it was confirmed the sphere is hollow which can act as an ‘ion reservoir’ to shorten ion diffusion length. The high-magnification SEM of the microsphere shown in Fig. 1d demonstrates that the spheres were composed of thickset nanosheets with an average thickness of ~20 nm which cross each other, leaving numerous open spaces and cavities among the nanosheets, which are beneficial for electrolyte to diffuse [17, 18].

From the TEM image of individual NiO sphere (Fig. 2a), we can further identify the hollow structure of NiO ball-flowers. Enlarged TEM image (Fig. 2b) demonstrates that the hollow NiO ball-flowers are assembled by numerous nanoparticles with a size around 5–10 nm, leaving mesoporous among the nanoparticles, which can facilitate the complete contact and faradaic reaction between the active material and electrolyte [19]. In the HRTEM image of NiO nanocrystals (Fig. 2c), the lattice fringes with *d*-spacing of 0.21 and 0.24 nm which assigned to the respective (200) and (111) planes of cubic NiO can be observed, further confirming the crystal structure of the as-synthesized NiO. This result is in accord with that from the previous reports [20, 21]. The corresponding typical selected area electronic diffraction (SAED) pattern (Fig. 2d) shows diffuse rings, which correspond to the (111), (200), (220), (311), (222) and (400) planes, manifesting the NiO ball-flowers are polycrystalline in nature.

To further describe the porosity of as-synthesized hollow NiO ball-flowers, the BET nitrogen adsorption–desorption isotherm of the as-prepared sample is depicted in Fig. 3a. It can be seen that the NiO sample exhibits the type IV isotherm with a distinct hysteresis loop in the range of 0.5–1.0 *P/P*₀, indicating the mesoporous structure. The BET surface area value and pore volume of the NiO ball-flowers are calculated to be 163.1 m² g⁻¹ and 0.376 cm³ g⁻¹. The corresponding pore size distribution centered at around 8.4 and 12.1 nm is calculated by BJH method from the

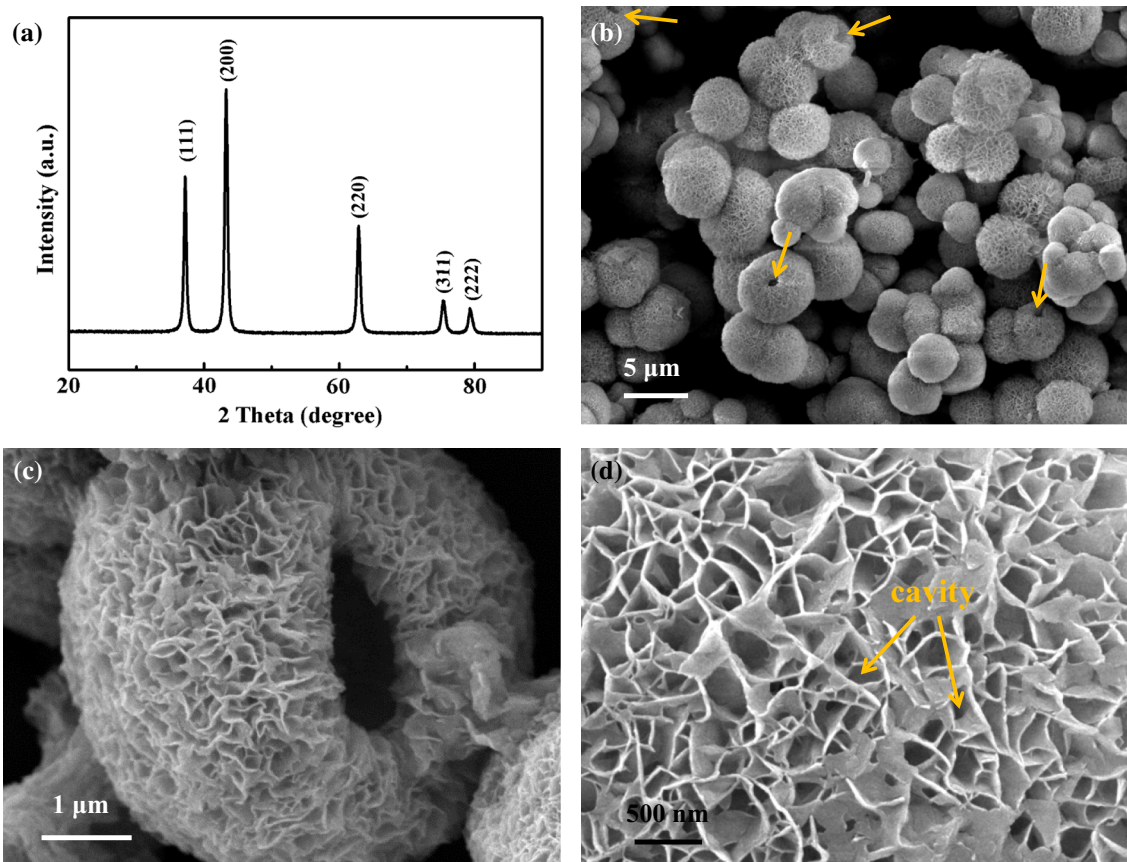
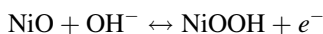


Fig. 1 a XRD patterns of as-synthesized NiO. b–d Low-, medium- and high magnification SEM images of as-prepared NiO hollow ball-flower

desorption branch as shown in Fig. 3b, determining a mean pore diameter of 10.8 nm. The large specific surface area and suitable pore size which correspond to the results of SEM and TEM can facilitate the solvent penetration of electrolyte and the faradaic reaction, improving the electrochemical performance [13, 19].

3.2 Electrochemical performances

The pseudocapacitor properties of hollow hierarchical NiO ball-flowers are elucidated by CV and GCD measurements in 6 M KOH solution as electrolyte. The CV curves (Fig. 4a) of as-synthesis hollow NiO at different scan rates show obvious redox reaction due to the conversion between NiO and NiOOH, which occurs at the surface of NiO electrode materials according to the following equation [10]:



With the increasing of scan rate, the oxidation and reduction peaks shift to higher and lower potential respectively, which is due to the increase of the internal diffusion resistance within the NiO materials, and the CV curves become more anamorphic, resulting from the limitation of

the ionic diffusion rate to satisfy electronic neutralization during the redox reaction [22–24].

Figure 4b shows the GCD curves of the as-prepared NiO at the discharge current densities of 1, 3, 5, 10 and 20 A g⁻¹ within the potential window between 0 and 0.45 V. The special charge–discharge curve which is nonlinear exhibits the characteristic of metallic oxides, and it further verifies the pseudocapacitance properties of the NiO electrode [25]. The specific capacitances were calculated from the following equation [26, 27]:

$$C = \frac{I \times \Delta t}{m \times \Delta v}$$

where I (A) is the discharge current, Δt (s) is the discharge time, m (g) is the mass of electrode material, and Δv (V) is the discharging potential range.

Based on the GCD curves of as-prepared hollow hierarchical NiO ball-flowers, the summary plot of specific capacitance versus the current density is shown in Fig. 4c. The specific capacitance values of the hollow NiO ball-flowers are 734, 726, 704, 600 and 484 F g⁻¹ at the current densities of 1, 3, 5, 10 and 20 A g⁻¹, respectively. With an increase of scan rate, it was observed the specific capacitance value decrease. The reduction of specific capacitance

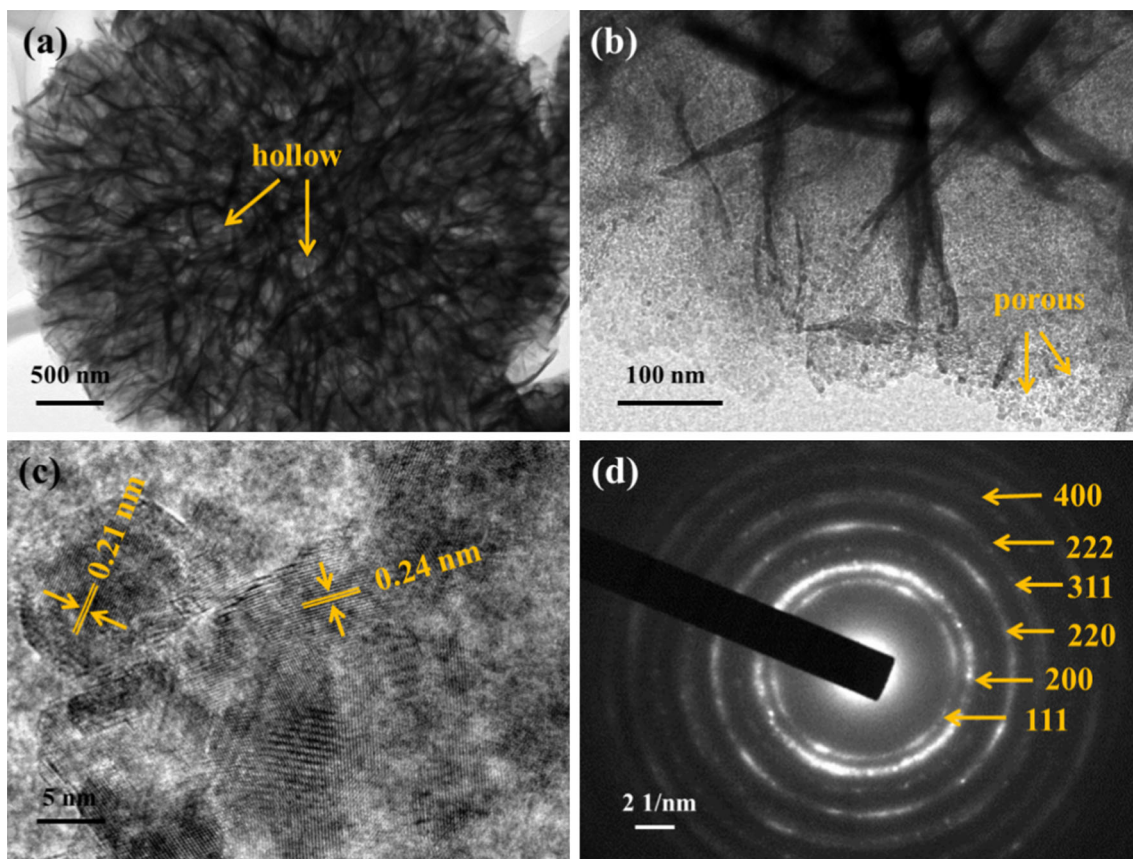


Fig. 2 TEM images (a, b), HRTEM image (c) and the corresponding SAED patterns (d) of the as-synthesized NiO

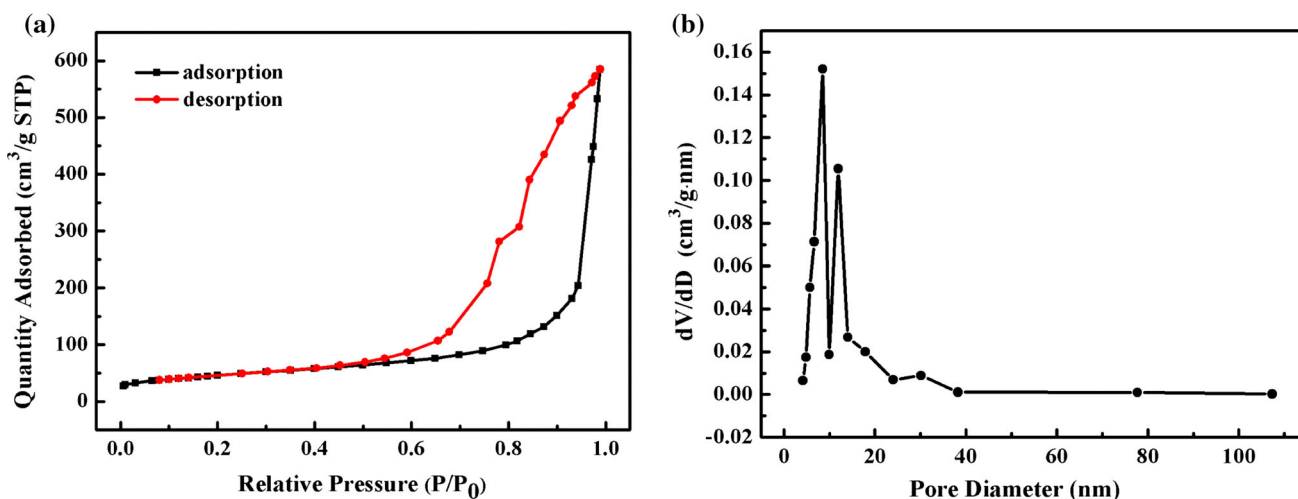


Fig. 3 N₂ adsorption–desorption isotherm (a) and pore-size distribution (b) of as-prepared NiO

at high rate can be attributed to the limitation of the ionic diffusion rate. During the high-rate charge–discharge process, only the outer active surface is utilized for faradaic reaction [28]. These obtained specific capacitance values of as-prepared hollow NiO ball-flowers are higher than those obtained from other NiO nanoparticles [29], NiO

nanoflakes [30], 3D hierarchical porous NiO [31], suggesting that these hollow NiO ball-flowers have excellent rate capability for supercapacitors. The good electrochemical performance may be attributed to the following factors. For one thing, the architecture of as-synthesized NiO is characterized by hollow, porosity and hierarchical

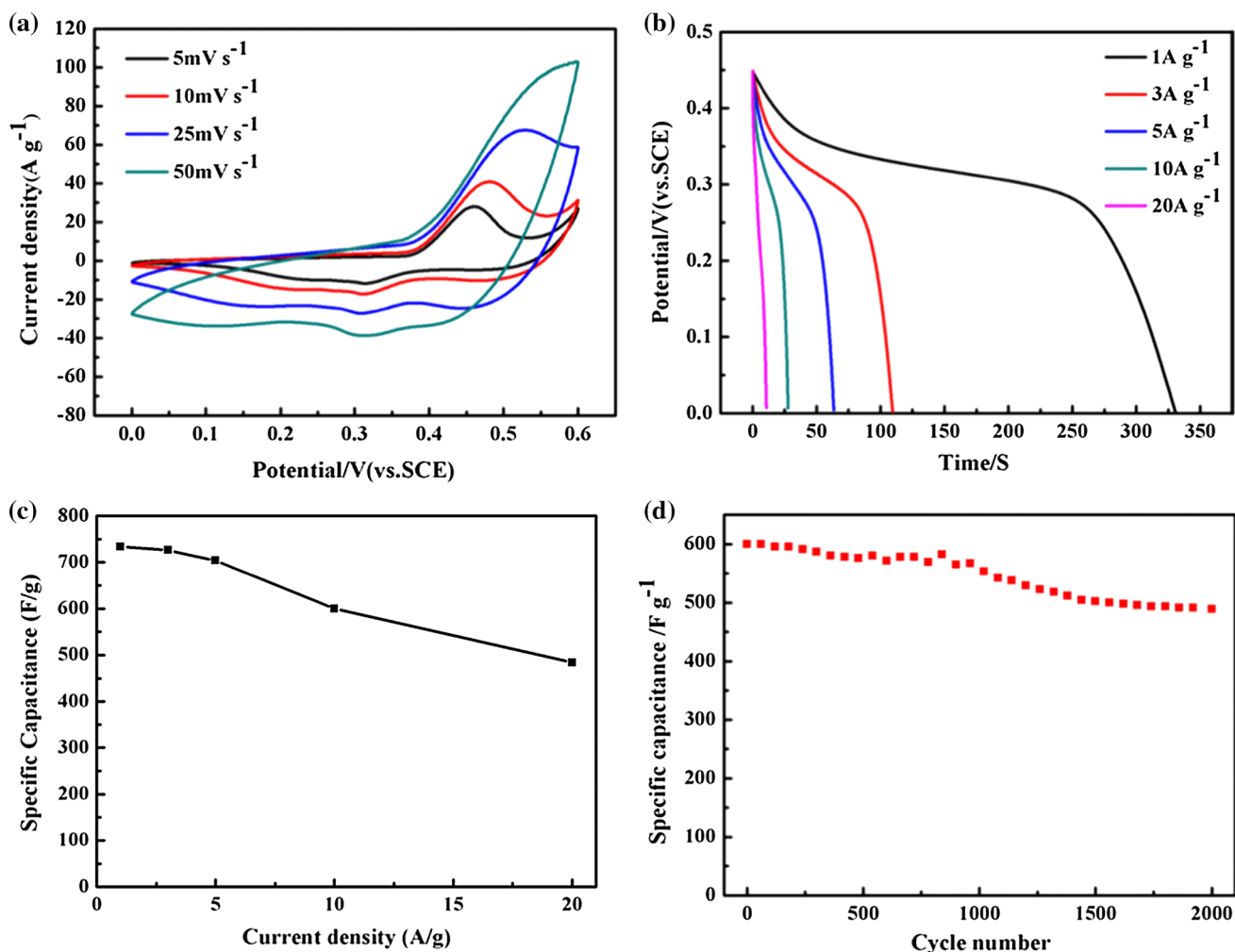


Fig. 4 **a** CV curves at different scanning rates, **b** GCD curves at different current densities, **c** specific capacitance versus current densities, and **d** cycling performance at 10 A g⁻¹ of as-prepared NiO hollow ball-flower

structure, which can provide a large specific surface area and more active sites, and facilitate the contact between the electrode and electrolyte, shorten ion diffusion length, leading to an enhanced capacitance [13]. For another, the numerous cavities left by the assembled nanosheets and the hollow structure can serve as the “ion reservoir” to deliver electrolytes to the interior of active materials, and improve the intercalation/deintercalation of ions, enhancing the utilization of active materials [19].

The cycling performance of the NiO sample is shown in Fig. 4d. After 2000 cycles, the as-synthesized NiO presents excellent specific capacitance of 489 F g⁻¹ at high current density of 10 A g⁻¹, which is about 82 % capacitance retention. The excellent cycling stability may be attributed to the nanosheet-assembled hollow structure which has the advantages of accommodating the volume changes during charge–discharge process [9].

To further examine the fundamental electrochemical behavior of the NiO ball-flowers, EIS analysis for the electrode material before and after suffering 2000 cycles was measured. The corresponding Nyquist plots which are composed of a nearly straight line in the low-frequency region and a semicircle in the high-frequency region are shown in Fig. 5. The intercept of plot on the real axis in the high frequency range represents the solution resistance (R_s) which includes the bulk resistance of the electrolyte, inherent resistances of the active material, and contact resistance at the interface between active material and current collector [32]. Faradaic charge transfer resistance (R_{ct}) can be calculated from the diameter of semicircle in the high frequency range [33]. The slope of the impedance plot in the low frequency range represents the Warburg impedance (W) which describes the ion diffusion behavior in the electrolyte and electrode [34]. The measured EIS are

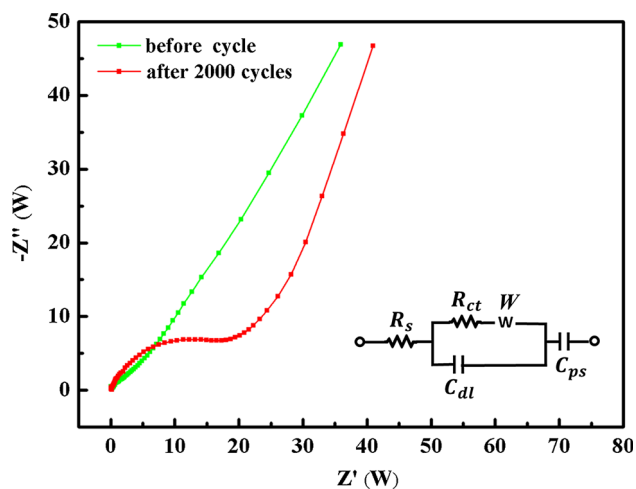


Fig. 5 EIS spectra of hollow NiO ball-flower before and after 2000 cycles of charge–discharge

analyzed and fitted using a standard model base on the equivalent circuit (inset of Fig. 5), where C_{dl} is a constant phase element accounting for a double-layer capacitor, and C_{ps} is a pseudocapacitive element. It can be observed that the NiO electrode after 2000 cycles shows a smaller W than that before 2000 cycles. Although the fitted R_s (0.52 Ω) of cycled NiO electrode is slightly bigger than that of the NiO (0.18 Ω) before 2000 cycles, the cycled NiO exhibits much larger R_{ct} (16.68 Ω) compared with the R_{ct} values of NiO (2.45 Ω) before 2000 cycles, leading to a capacity fading during the cycling process. As the charge transfer resistance is usually influenced by the intrinsic resistance of the electrode material, ionic resistance of electrolyte, and the contact resistance between the active material and current collector, it may be the loose of active material coated on the current collector, which enlarge the charge transfer resistance, leading to the fading of electrochemical performance [35, 36]. The EIS analysis result is also consistent with the charge–discharge cyclic performance of as-prepared hollow NiO ball-flowers.

4 Conclusions

In summary, hollow NiO ball-flowers assembled by porous nanosheets were prepared through a facile and template-free hydrothermal route. The unique NiO nanostructure with characteristic of hollow, porosity and hierarchical structure, was applied to supercapacitor as electrode materials, which has a BET surface area as high as 163.1 $\text{m}^2 \text{g}^{-1}$, exhibiting high specific capacity of 734 F g^{-1} at 1 A g^{-1} as well as an excellent capacitance retention of 82 % after 2000 cycles. Based on the above analysis, the hollow NiO ball-flowers are promising candidate as electrode material which can be applied to supercapacitor.

Acknowledgments This work was supported by the National Natural Science Foundation of China (No. 51302328) and supported in part by the Fundamental Research Fund for the Central Universities (No. 106112015CDJXY130006).

References

1. M. Yao, Z. Hu, Y. Liu, P. Liu, Z. Ai, O. Rudolf, J. Alloys Compd. **648**, 414–418 (2015)
2. G. Wang, L. Zhang, J. Zhang, Chem. Soc. Rev. **41**, 797–828 (2012)
3. Y. Jiang, X. Leng, Z. Jia, H. Chen, H. Suo, C. Zhao, J. Mater. Sci. Mater. Electron. **26**, 2995–3000 (2015)
4. D. Xie, Q. Su, Z. Dong, J. Zhang, G. Du, CrystEngComm **15**, 8314–8319 (2013)
5. Y. Zhang, J. Wang, H. Wei, J. Hao, J. Mu, P. Cao, J. Wang, S. Zhao, Mater. Lett. **162**, 67–70 (2016)
6. Z. Yang, F. Xu, W. Zhang, Z. Mei, B. Pei, X. Zhu, J. Power Sources **246**, 24–31 (2014)
7. F. Cao, G.X. Pan, X.H. Xia, P.S. Tang, H.F. Chen, J. Power Sources **264**, 161–167 (2014)
8. D. Wei, Z. Xu, J. Liang, X. Li, Y. Qian, J. Mater. Sci. Mater. Electron. **26**, 6143–6147 (2015)
9. L. Hu, Q. Chen, Nanoscale **6**, 1236–1257 (2014)
10. M. Khairy, S.A. El-Safty, RSC Adv. **3**, 23801–23809 (2013)
11. A. Xiao, S. Zhou, C. Zuo, Y. Zhuan, X. Ding, Mater. Res. Bull. **61**, 54–57 (2015)
12. Y. Zhang, L. Li, H. Su, W. Huang, X. Dong, J. Mater. Chem. A **3**, 43–59 (2015)
13. F. Shi, L. Li, X.-L. Wang, C.-D. Gu, J.-P. Tu, RSC Adv. **4**, 41910–41921 (2014)
14. Z. Cui, H. Yin, Q. Nie, D. Qin, W. Wu, X. He, J. Electroanal. Chem. **757**, 51–57 (2015)
15. X.H. Huang, J.P. Tu, C.Q. Zhang, F. Zhou, Electrochim. Acta **55**, 8981–8985 (2010)
16. M. Huang, X.L. Zhao, F. Li, W. Li, B. Zhang, Y.X. Zhang, J. Mater. Chem. A **3**, 12852–12857 (2015)
17. Q. Yang, Z. Lu, T. Li, X. Sun, J. Liu, Nano Energy **7**, 170–178 (2014)
18. Q. Wu, Y. Liu, Z. Hu, J. Solid State Electrochem. **17**, 1711–1716 (2013)
19. X. Liu, J. Zhao, Y. Cao, W. Li, Y. Sun, J. Lu, Y. Men, J. Hu, RSC Adv. **5**, 47506–47510 (2015)
20. G.H. Yue, Y.C. Zhao, C.G. Wang, X.X. Zhang, X.Q. Zhang, Q.S. Xie, Electrochim. Acta **152**, 315–322 (2015)
21. V. Senthilkumar, F.B. Kadumudi, N.T. Ho, J.-W. Kim, S. Park, J.-S. Bae, W.M. Choi, S. Cho, Y.S. Kim, J. Power Sources **303**, 363–371 (2016)
22. W. Yu, X. Jiang, S. Ding, B.Q. Li, J. Power Sources **256**, 440–448 (2014)
23. G. Cheng, W. Yang, C. Dong, T. Kou, Q. Bai, H. Wang, Z. Zhang, J. Mater. Chem. A **3**, 17469–17478 (2015)
24. Y. Zhang, Y. Liu, Y. Guo, Y.X. Yeow, H. Duan, H. Li, H. Liu, Mater. Chem. Phys. **151**, 160–166 (2015)
25. H. Xiao, F. Qu, X. Wu, Appl. Surf. Sci. **360**, 8–13 (2016)
26. W. Han, L.-B. Kong, M.-C. Liu, D. Wang, J.-J. Li, L. Kang, Electrochim. Acta **186**, 478–485 (2015)
27. W. Chen, X. Tao, D. Wei, H. Wang, Q. Yu, Y. Li, J. Mater. Sci. Mater. Electron. **27**, 1357–1362 (2015)
28. M. Kuang, W. Zhang, X.L. Guo, L. Yu, Y.X. Zhang, Ceram. Int. **40**, 10005–10011 (2014)
29. T. Meng, P.-P. Ma, J.-L. Chang, Z.-H. Wang, T.-Z. Ren, Electrochim. Acta **125**, 586–592 (2014)

30. X. Yan, X. Tong, J. Wang, C. Gong, M. Zhang, L. Liang, J. Alloys Compd. **593**, 184–189 (2014)
31. J. He, Y. Zhao, D.-B. Xiong, W. Ran, J. Xu, Y. Ren, L. Zhang, Y. Tang, F. Gao, Mater. Lett. **128**, 117–120 (2014)
32. S. Khalid, C. Cao, A. Ahmad, L. Wang, M. Tanveer, I. Aslam, M. Tahir, F. Idrees, Y. Zhu, RSC Adv. **5**, 33146–33154 (2015)
33. M.S. Kolathodi, M. Palei, T.S. Natarajan, J. Mater. Chem. A **3**, 7513–7522 (2015)
34. E. Umeshbabu, G. Rajeshkhanna, G.R. Rao, Int. J. Hydrogen Energy **39**, 15627–15638 (2014)
35. M. Fan, B. Ren, L. Yu, D. Song, Q. Liu, J. Liu, J. Wang, X. Jing, L. Liu, Electrochim. Acta **166**, 168–173 (2015)
36. X. Dai, D. Chen, H. Fan, Y. Zhong, L. Chang, H. Shao, J. Wang, J. Zhang, C.-N. Cao, Electrochim. Acta **154**, 128–135 (2015)